DOI: 10.13009/EUCASS2019-559

8TH EUROPEAN CONFERENCE FOR AERONAUTICS AND AEROSPACE SCIENCES (EUCASS)

DOI: ADD DOINUMBER HERE

Influence of numerical model setup on the response of acoustically forced LOx/H_2 flames

Federica Tonti[⋆†], *Justin S.Hardi*[⋆], *Tim Horchler*[♣], *Stefan Fechter*[♣] *and Michael Oschwald*[⋆]
[⋆]*German Aerospace Center (DLR)-Institute of Space Propulsion Lampoldshausen, Hardthausen, 74239, Germany*
[♣]*German Aerospace Center (DLR)-Institute for Aerodynamics and Flow Technology, 37073 Göttingen, Germany*
First Author Email: federica.tonti@dlr.de · Second Author Email: justin.hardi@dlr.de
[†]Corresponding author

Abstract

The current work aims to study the influence of the numerical setup on a URANS model of a single co-axial injection element under acoustic forcing. The single injector model is representative of an experimental rocket combustor with multiple injection elements, named BKH and operated at DLR Institute of Space Propulsion. The configurations presented in this work are fully 3D for the 1L and 1T mode excitation and compared with previous configurations.[14,34]The flame zone is studied with an unstructured and hybrid mesh. An influence of the numerical setup is visible.

1. Introduction

High frequency combustion instabilities have been a key issue in the development of liquid rocket engines since the very first attempts of their design and building in the 1950's.[5] Despite this, they are not yet fully understod and their occurrence cannot be predicted. This phenomenon consists of high amplitude pressure oscillations which can occur in the combustion chamber of a liquid rocket engine, taking the form and frequencies of the resonant modes of the chamber itself and being driven by the coupling between acoustic pressure oscillations and unsteady energy release from the combustion process. This coupling leads to a fluctuating heat release rate and these phenomena close in a loop. More specifically, we refer to this mechanisms as thermoacoustic combustion instabilities in which essentially the following specific physical process are involved: the feedback between heat release fluctuations (or flame fluctuations) with the combustor or combustion chamber acoustics, the coupling of these two processes in space-time, the strength of this coupling in comparison with acoustic losses, and the physical mechanisms behind the heat release fluctuations. If these fluctuations are in phase with the pressure fluctuations, the acoustic fluctuation can reach levels which could also lead to the failure of the chamber, and so of the entire mission.[21,40]
Proper numerical tools are necessary to gain further insights into the physical and chemical processes involved in the occurrence of combustion instabilities. After a validation against experimental data, numerical tools like CFD can be employed to better understand experimental findings and eventually used as predictive tool for combustion instabilities. Direct numerical simulations (DNS), large eddy simulations (LES) and Unsteady Reynold Averaged Navier Stokes equations simulations (URANS) have been able to give insights into several mechanisms which occur in transcritical and supercritical coaxial cryogenic flames.[3,4,17,20,39]Simulation and experiments have demonstrated that a flame under acoustic excitation can release a considerable amount of heat due to its movement and the fluctuating pressure inside the chamber. The obtained heat release rate distributions can be used to estimate driving and damping contributions to the Rayleigh term or to build flame response functions.[11,12,28]
The focus of this work is the experimental combustor BKH, which operates with LOx and H_2. BKH optical data have been previously analysed by Beinke in[34,35] to identify the flame response to longitudinal and transverse acoustic excitation and to produce results useful for numerical validation. An unsteady model of a single BKH injection element subjected to an acoustic disturbance with a representative distribution of the field produced by exciting the first longitudinal chamber mode was already proposed by Tonti,[14] and a corresponding model for the excitation of the first transverse mode was proposed by Beinke.[27] Here the influence of the numerical setup is studied, investigating the influence of the axisymmetry boundary condition applied to the previous configurations by modifying the geometry from a 2D to a 3D cylindrical domain for the acoustic pressure excitation, and doubling a half domain to a full 3D domain for the transverse velocity excitation. Two different mesh configurations for each case are investigated: a

DOI: 10.13009/EUCASS2019-559

fully unstructured mesh, and a hybrid structured/unstructured mesh. The results of the different configurations are then compared with previous experimental and numerical data.

2. Numerical Modelling

The investigation of the flame response to an imposed acoustic disturbance of the BKH study elements has been conducted using a single injector model, representative of the central element in the primary injection confguration. In house DLR-TAU code is used to perform the simulations. As a first step, steady-state calculations of the different numerical setup are conducted. Subsequently, two different acoustic perturbations are modelled and applied using an URANS approach. During the unsteady calculations, the boundary conditions of the domain are modified to impose the representative acoustic disturbance on the single injection element. In the following subsections, the DLR TAU code, numerical domain, boundary conditions and excitation modelling are described.

2.1 CFD Solver

The DLR TAU code is a hybrid (structured/unstructured) grid Godunov-type finite-volume flow solver for the compressible Euler and Navier-Stokes equations. Spatial second order is reched by a MUSCL reconstruction. DLR TAU code has been validated for a range of steady and unsteady flow cases.[1,9,37]
A MAPS+ Riemann solver by Rossow[32] is used to handle low Mach number flows and high density gradients, which are challenging for a compressible flow solver. An explicit 3rd order Runge-Kutta scheme is used for time integration. To perform unsteady computations a Jameson-type dual time stepping scheme is used, with a physical time step size of $5x10^{-6}$ s. To assure convergence for each time step, a Cauchy convergence control method for each simulation is employed.
The operating conditions are the same for both pressure and transverse velocity excitation. They are summarized in Table 1. A turbulent Schmidt number of 0.3 and a ratio between laminar and turbulent Prandtl number of 0.8 was used. The choice of these values is due to the good match that they give with experimental data, as assessed for example in He et al.[22] and Turker at al.[38]

Table 1: Operating conditions

ROF	6
Mean chamber pressure	60 bar
Oxygen Temperature at injection	127 K
Hydrogen Temperature at injection	279 K

The one-equation Spalart-Allmaras turbulence model[36] is used, due to its robustness and ease of implementation.
A six-species and seven-step reaction scheme for oxygen-hydrogen combustion published by Gaffney et al[15] that includes the species H_2, O_2, H, O, OH and H_2O was employed.
Cryogenic propellants at high pressures, as in rocket engines, behave differently than ideal gases and this has to be taken into account. These real-gas effects are included in the DLR TAU code real gas release to model injection and combustion of cryogenic propellants. This real gas implementation has two main features: each species has a dedicated equation of state and the properties of the mixture are determined by a multi-fluid mixing model.[6,7,10] Here the ideal gas equation of state is solved for H_2, H, O, OH and H_2O, and a real gas equation of state is solved for O_2. The real gas transport properties of oxygen are computed form the high fidelity EOS for O_2 as proposed by Lemmon et al.[29] In the current release of TAU code, an adaptive tabulation of high-accuracy equation of state (EOS) is used, first introduced by Dumbser et al.[30] for cavitating flows. In the context of the mixture description within the TAU code the tabulation idea has been extended by Fechter et al.[13] for the application within ideal gas mixtures. The assumption of ideal gas mixing of species properties is valid only if all species exist as a real-gas in only a pure-fluid state. This assumption is physically justified if we focus on supercritical oxygen-hydrogen combustion. Numerical studies by Oefelein[4,25] have noted the flame produced by a coaxial injection element in an oxygen-hydrogen liquid propellant rocket engine effectively isolates the fuel and oxidizer streams. This agrees with similar experimental observations made by Oschwald et al.[31] and many others. Numerical studies of representative reacting cryogenic shear layers by Bellan[24] and 1D counter diffusion flames by Ribert et al.[18] and Lacaze et al.[16] have shown that mixing in the hot reaction zone occurs under ideal gas conditions.
Banuti et al.[8] further explain that all real fluid effects are essentially confined to the LOx core under supercritical O_2/H_2 combustion conditions. Thus for the flames considered in the present work, the multi-fluid ideal-mixing model is appropriate. The fluid in the numerical domain is assumed to exist as either a pure-fluid real-gas or a mixture that can

DOI: 10.13009/EUCASS2019-559

be approximated using an ideal-mixing model. The fluid is treated as a continuous Eulerian mixture with no discrete phases or phase changes. This approach is sometimes referred to as an Euler-Euler model.

2.2 Excitation Modelling

The single injector configurations are acoustically excited by modulating the boundary conditions at the sides of the domain. In particular, for the unsteady calculations, the side boundaries are specified as nearfield boundary conditions, modified at each time step in order to impose the acoustic disturbance. The nearfield boundary condition is used to represent here a fluid boundary and it defined by specifying the mixture properties at the boundary surface. To impose the disturbance, the dynamic fluctuation is superimposed to a mean value given from the steady state simulation and then imposed at the nearfield boundaries. The state of the nearfield boundaries is updated at each time step. To model a realistic 1L mode acoustic disturbance, both a pressure and velocity fluctuations about the steady-state values are imposed.

$$p = \bar{p} + p' \tag{1}$$

$$v = \bar{v} + v' \tag{2}$$

where $\bar{p}$ is the steady state value of pressure, p' is the pressure fluctuation about that value, $\bar{v}$ is the steady state value of the velocity and v' is the fluctuation about the steady state value. The expression for the imposed acoustic disturbance is:

$$p' = Ae^{i\omega t} \tag{3}$$

$$v' = \frac{i}{\rho\omega}\nabla\hat{p}e^{i\omega t} \tag{4}$$

where A is the magnitude of the amplitude of the pressure disturbance, ρ is the density and ω=$2\pi f$ where f is the excitation frequency.
To model the 1T mode excitation, the transverse pressure disturbance is prescribed as a function of the vertical coordinate of the domain y, the height of the domain H and the desired amplitude of the pressure fluctuation at the wall $Re(|p'_{wall}|)$, wich is the real part of $|p'_{wall}|$:

$$p' = Re(|p'_{wall}|)\sin\Big(\frac{y\pi}{H}\Big)e^{i\omega t} \tag{5}$$

The transverse velocity disturbance is then computed to match the imposed pressure disturbance and written in the form of equation 4, leading to:

$$v' = \frac{Re(|p'_{wall}|}{2\rho f H}\cos\Big(\frac{y\pi}{H}\Big)e^{i(\omega t+\pi/2)} \tag{6}$$

Representations of the applied disturbances are given in Figure 1. The investigated test cases in terms of amplitude and frequencies of the disturbances for both cases are summarized in Table 2.

Table 2: Investigated cases

	1L	**1T**
Amplitude of disturbance ($\%\ of\ p_{cc}$)	5%	3.5%
Frequency of disturbance (Hz)	3200	4400
	3400	

DOI: 10.13009/EUCASS2019-559

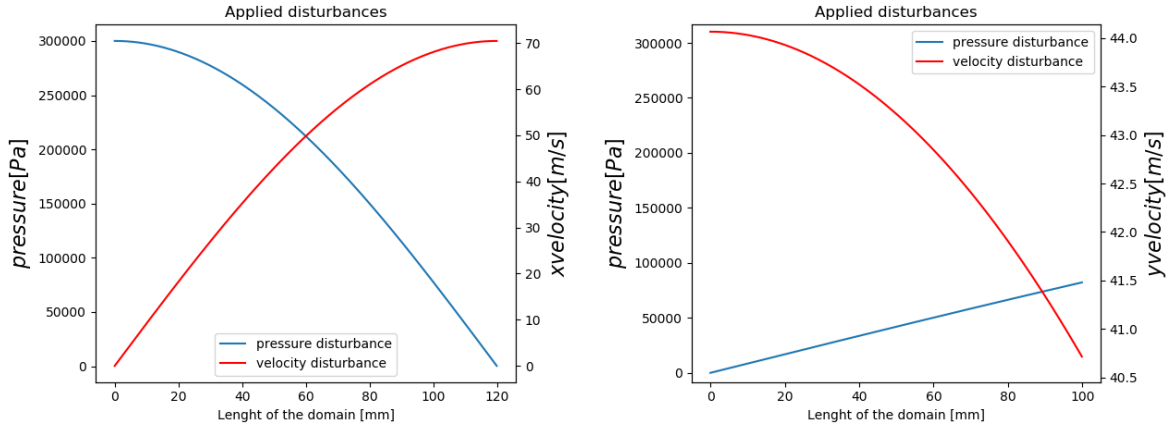

(a) Imposed pressure disturbance (1L mode)

(b) Imposed transverse velocity disturbance (1T mode)

Figure 1: Axial distribution of the applied disturbances on the domain boundary

3. Numerical Results

3.1 Pressure excitation

3.1.1 Numerical domain and boundary conditions

Two different geometries are considered. The first one is a 2D axisymmetric domain, chosen because the imposed disturbance should act symmetrically about the flame and not disturb the flame from the centerline of the injector. LOx post has been included in the domain to observe the LOx post coupling, identified as a possible source of instabilities in oyxgen-hydrogen rocket engines, experimentally by Gröning et al.[19] and numerically by Urbano et al.[2] and Hardi et al.[26] The chosen boundary conditions are mass flow rate specified at the oxygen and hydrogen inlet to match the operating conditions of oxidizer to fuel mass flow rate (ROF) of 6 and chamber pressure of 60 bar. The LOX post walls, injection plane and throttle section are specified as viscous walls, to the outlet of the domain a farfield boundary condition specifying the chemical composition, density, velocity and temperature of the mixture, calculated with the NASA software CEA as an equilibrium mixture of combustion products at the prescribed chamber pressure. This boundary condition is used to control the pressure inside the volume.
For the steady-state calculations, an inviscid wall boundary condition is specified at the side boundaries. Figure 2(a) displays the geometry of the domain and the applied boundary conditions. The boundary conditions implemented in TAU are described by Horchler et al.[23] The second configuration consists in a cylindrical geometry obtained by rotating the 2D geometry around the axisimmetry axis of 360°. The boundary conditions are the same of the 2D configuration, except for the axisymmetry boundary condition, which here is not applied. This way, an investigation about the influence of the axisymmetry boundary condition is performed. Figure 2(b) shows the domain and boundary conditions of the 3D configuration.
For the 2D axisymmetrical geometry, an unstructured grid is used. The mesh has about 0.16 M nodes, with size of elements varying from 0.03 mm in the shear layer to 0.5 mm at the end of the domain. The mesh is refined in the region of the post tip, in the shear layer between the hydrogen and oxygen streams, as shown in Figure 3.
For the 3D geometry, two mesh configurations are used: a fully unstructured mesh and a hybrid structured/unstructured mesh. The fully unstructured mesh has about 0.8 M nodes, whereas the hybrid mesh has about 0.7 M nodes. The hybrid mesh has two hexahedral blocks, one in the LOx post and one in the flame zone. The interface between the injection and the flame zone is filled with an unstructured grid of the same density as for the unstructured one, up to 4 mm downstream the LOx injector, where then the mesh is switched to structured elements with coarser distribution. In this way, a good resolution both for transition and flame zone is provided, as well as a considerable gain in terms of number of nodes.

3.1.2 Steady state results

In this section, a comparison of the steady-state results for the different configurations is performed. A steady state RANS is carried for each of the three configurations. Figure 5 shows the density isosurfaces for $\rho = 10\ kg/m^3$ and $\rho = 100\ kg/m^3$, OH mass fraction and temperature distributions.

DOI: 10.13009/EUCASS2019-559

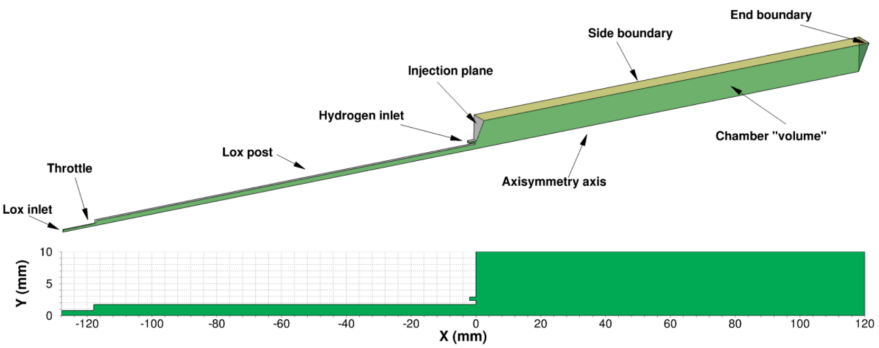

(a) 2D domain

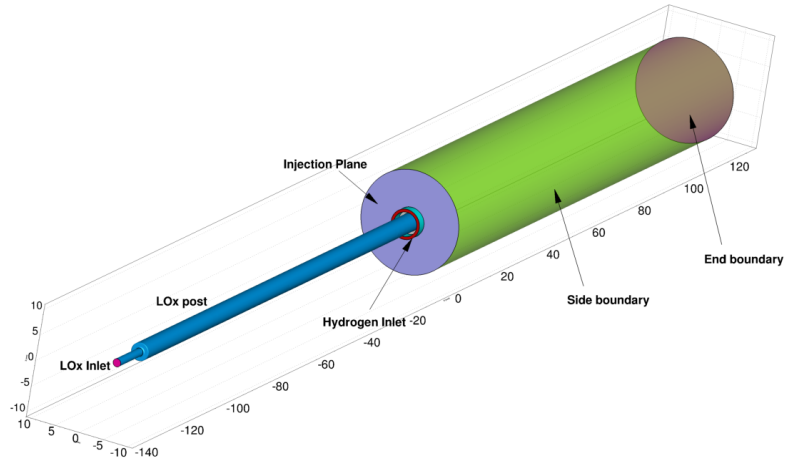

(b) 3D domain

Figure 2: Domains and boundary conditions used for the pressure excitation calculations.

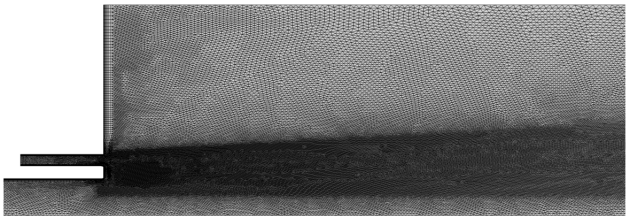

Figure 3: Mesh detail at injection

From Figure 5(a), a clear difference in the length of the LOx core between the three cases is visible.The hybrid mesh shows a longer LOx core with respect to the fully unstructured mesh. This is due to the different meshing elements used in the LOx core zone: in the hybrid mesh, hexahedral elements are used, whereas in the fully unstructured mesh the same zone is filled with tetrahedra. Tetrahedral elements are suitable for complex geometries, but when the shape function is integrated with points of Gauss, they result to be less accurate than hexahedral elements and give a distortion of the mesh which is not present when dealing with hexahedral elements. In fact, hexahedral elements present a central symmetry. The possible loss of second order accuracy in truncation error for the Euler equations is localized on the boundaries of the cell and the first order error terms tend to cancel each other when averaged over several elements. As a result, the global solution error should remain second order.
It is possible, however, that this canceling of first order truncation error does not occur in viscous regions where second order derivatives of the flow variables play a significant role. If this is the case, then it will be necessary to maintain central symmetry of the control volumes in boundary layer regions for Navier-Stokes computations. More details about this topic can be found in Sadrehaghighi.[33] Essentially, when dealing with strong gradients, that occur e.g in shear or boundary layers, it is better to use hexahedral elements. This effect is clearly visible in Figure 5(c), where a detail

DOI: 10.13009/EUCASS2019-559

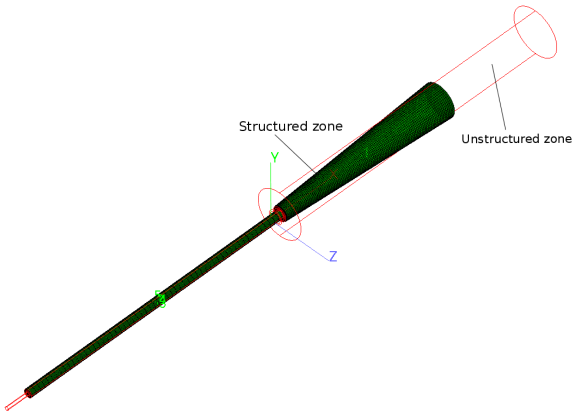

(a) Hybrid mesh

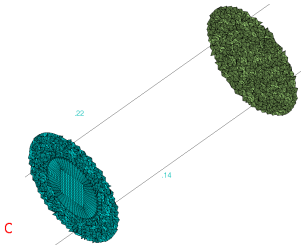

(b) Detail of chamber volume at locations x= 50 mm and x= 75 mm

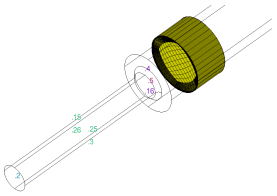

(c) Detail of Lox post at location x=-115mm

Figure 4: Hybrid mesh configuration

of the shear layer in the transition zone is shown. Despite having less nodes, the resolution of the shear layer is not affected, and a smoother transition to the fully developed flame is visible.
When comparing the 3D hybrid mesh solution to the 2D solution, also geometrical effects have to be taken into account. As shown in Figure 5, the 2D domain shows a longer and thinner LOx core and flame with respect to both 3D domains, because in the 2D geometry there is not the possibility of lateral spreading of the flux. An important role is played also by turbulence: mixing and diffusion phenomena are never purely 2D, and in RANS models 3D diffusion might be accounted for by the transport equation of turbulence quantities. Table 3 summarises the differences in the LOx core length, where L is the length of the intact LOx core and D is the diameter of the LOx injector.

Table 3: LOx core characteristics

	2D	**3D hybrid**	**3D unstructured**
LOx core length at $\rho = 100\ kg/m^3$)	62.42	56.2	53.23
LOx core length at $\rho = 10\ kg/m^3$)	64.33	60.48	56.54
L/D	≈18	≈16	≈15

3.1.3 Excitation results

In this section, an analysis of the steady state flow fields subjected to the 1L mode excitation is discussed. Figure 6(a) shows that, for all the cases, the amplitude of pressure oscillations at the tip of the flame along the axis once a steady regime is established for the 3200 Hz disturbance does not vary for the three cases. This means that there is no alteration of the excitation signal due to the different geometries or boundary conditions. The 2D configuration presents spurious pressure oscillations at the peak of the sinusoidal signal, whereas the 3D configurations do not. This can be observed also for higher excitation frequency (3400 Hz) in Figure 6(b). It can be then concluded that the axisymmetry boundary condition is the main cause of the spurious (numerical) pressure oscillations on the axis.
BKH flame subjected to 1L excitation presents a typical behaviour: the flame shows a wave like structure in the shear layer between the oxygen and hydrogen streams. Figure 7 shows a snapshot for the three configurations.

DOI: 10.13009/EUCASS2019-559

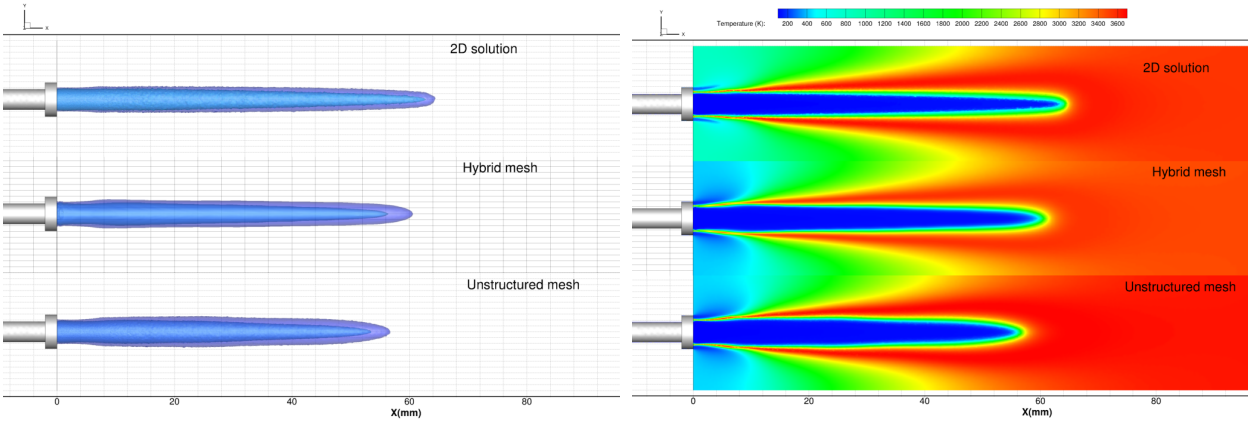

(a) (b)

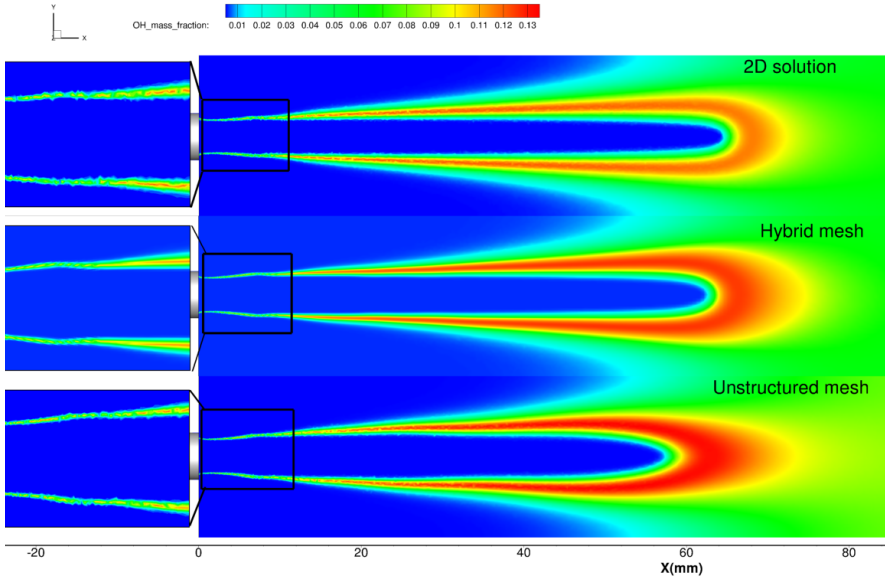

(c)

Figure 5: Density isosurfaces (5(a)) temperature (5(b)) and OH mass fraction distribution 5(c) for the three different configurations.

DOI: 10.13009/EUCASS2019-559

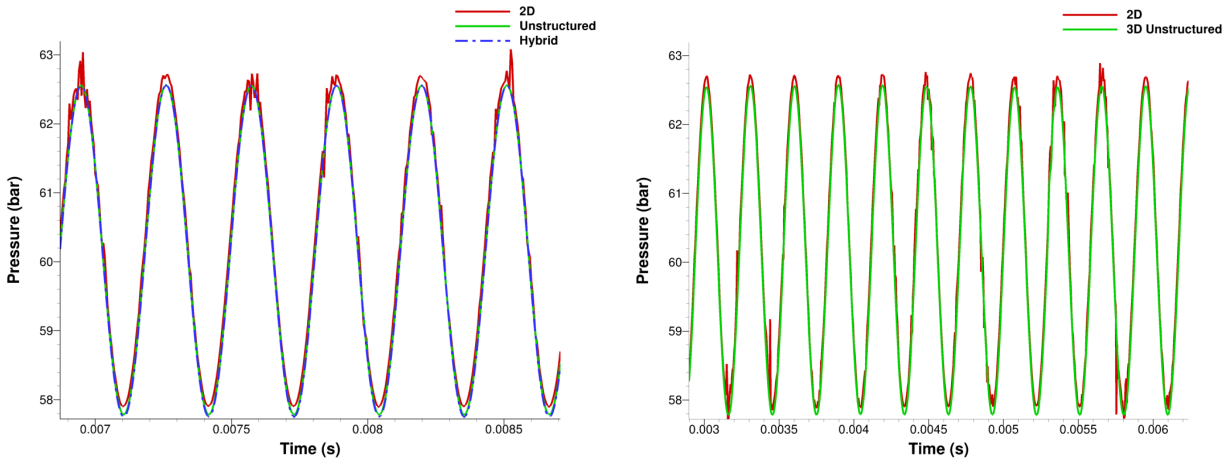

(a) (b)

Figure 6: Pressure fluctuations along the chamber axis at x=50 mm for the different configurations at f=3200 Hz 6(a) and f=3400 Hz 6(b)

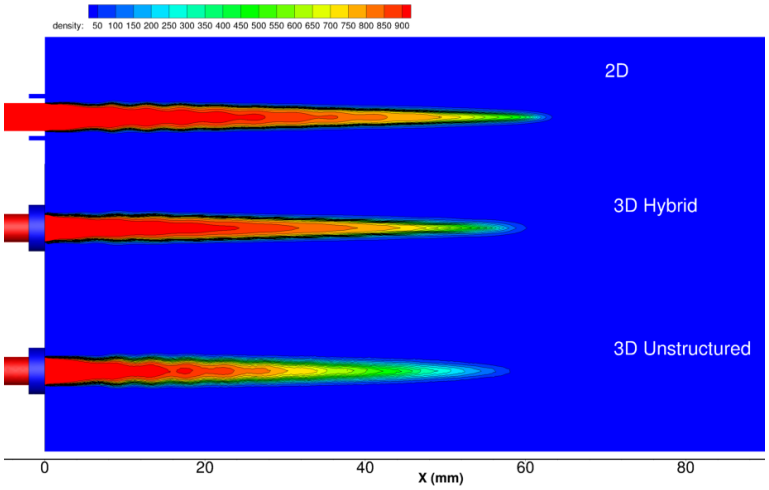

Figure 7: Density fields after 10 ms for the three configurations.

DOI: 10.13009/EUCASS2019-559

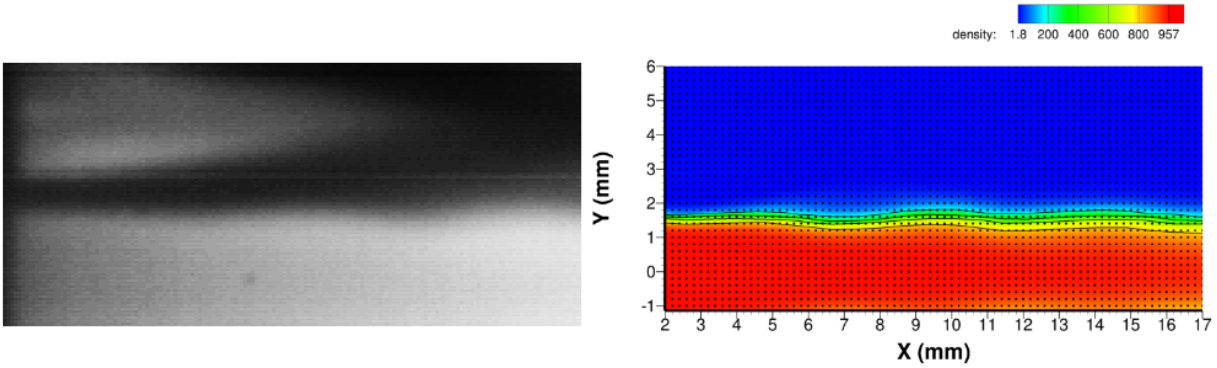

Figure 8: Qualitative comparison of the experimental data with numerical results

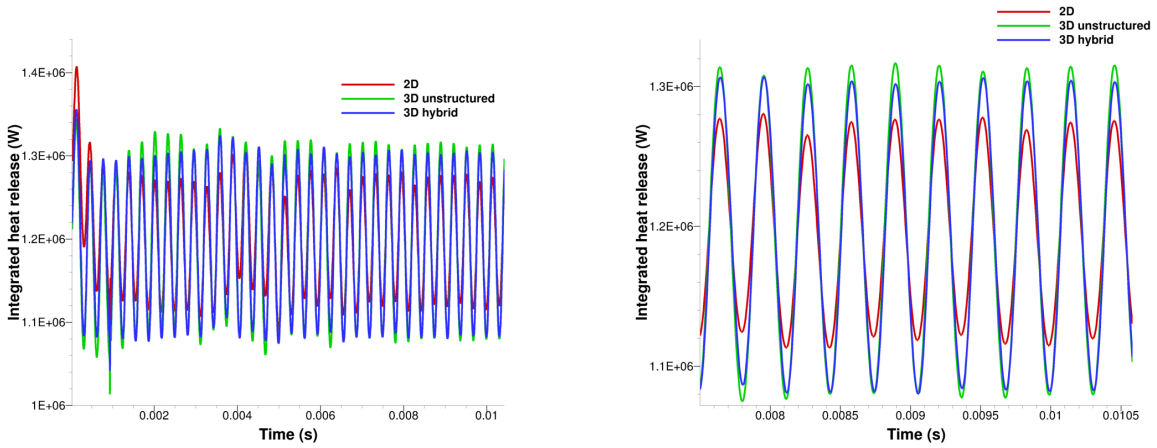

(a) Entire simulation

(b) Steady-state fluctuations

Figure 9: Evolution of the integrated heat release

Some differences appear: the 2D configuration is always the one which gives the longest LOx core. The hybrid mesh follows this trend, well reproducing this behaviour, whereas the unstructured mesh gives a shorter LOx core with pockets of dense oxygen detaching inside the core itself. It is interesting to notice, however, that the hybrid mesh tends to smooth the shear layer, giving a lower amplitude of the ripples, mantaining anyway the same spacing between crests and troughs. Moreover, the amplitude of the ripples in this case are in good agreement with the experimental data, as it can be seen Figure 8.
A key physical variable in high frequency combustion instabilities is the heat release rate. Figure 9(b) shows the heat release integrated over the volume for the three configurations. The relative fluctuations are summarised in Table 4.

Table 4: Heat release fluctuations (%) at $p' = 3$ bar $Frequency = 3200$ Hz

	2D	**3D hybrid**	**3D unstructured**
Difference of mean value [a]	+17.4%	+3.4%	+3.5%
Relative at steady-state fluctuations (peak-to-peak)	reference	+6%	+6%

[a]Compared to initial steady state solution

From the values given in the table, one can observe that, once reached steady state fluctuations, the 2D configuration presents lower heat release rate fluctuations with respect to both 3D configurations, which show approximately the

DOI: 10.13009/EUCASS2019-559

same values. This may be due to the axisymmetry boundary condition: in fact, this boundary condition is a first order one, whereas the solver follows second order spatial reconstruction. This could cause an underestimation of the integrated heat release when applying the axysymmetry boundary condition. For the disturbance at the same amplitude at a frequency of 3400 Hz, the same trend can be observed, with a peak-to-peak difference in the amplitude of the fluctuation of 6%.

3.2 Transverse velocity excitation

3.2.1 Numerical domain and boundary conditions

In order to study the response of BKH flames subjected to transverse acoustic velocity excitation a 3D domain is used. In this case, the 3D domain was necessary to capture the fluctuations and flattening of the flame subsequent to the applied excitation. The single injector model was excited with a one dimensional velocity disturbance. Two configurations are investigated. The first one is a configuration which exploits an axisymmetry boundary condition applied on the X-Y plane parallel to the imposed disturbance previously investigated by Beinke.[34] The other boundary conditions and the operating conditions are kept the same as for the acoustic pressure excitation case, for all the investigated configurations.
For the half box configuration, an unstructured grid was used, refined in the near injection region as in the 2D pressure excitation configuration, with about 0.6 M nodes. Nevertheless, the mesh is not as refined as in 2D configuration in the shear layer region to reduce computational costs. However, for the steady state solution the length of the flame and its shape are approximately the same, considering also the geometrical differences of the two domains. Figure 10 shows the boundary conditions and the mesh.

The second configuration presents a full 3D domain, not exploiting the axisymmetry boundary condition anymore. This is done in order to investigate the influence of this boundary condition on the flame response. For this last case, two mesh configurations are studied: a fully unstructured mesh, generated by simply mirroring the half domain mesh about the axisymmetry axis, and a hybrid mesh configuration. The unstructured mesh configuration has about 1.2 M nodes, whereas the hybrid one has about 1 M nodes. Figure 11 displays the configuration of the structured blocks used for the hybrid mesh.

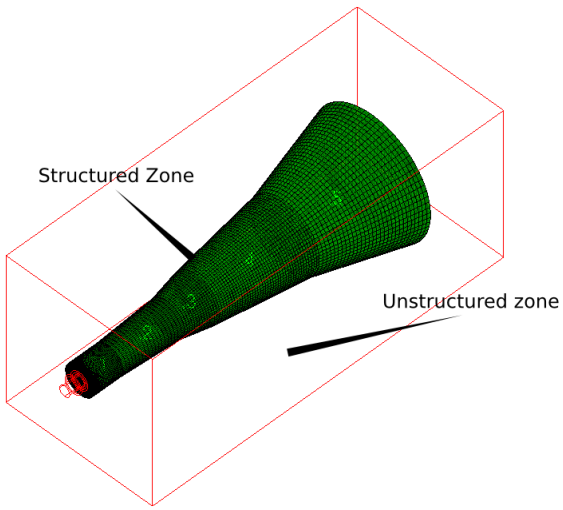

Figure 11: Hybrid mesh blocks configuration

Both hydrogen and oxygen injectors are in a pressure node during the excitation. This gives a limited coupling between the injection elements and the chamber, and consequently only a short segment of the hydrogen and oxygen posts are included in the domain.

DOI: 10.13009/EUCASS2019-559

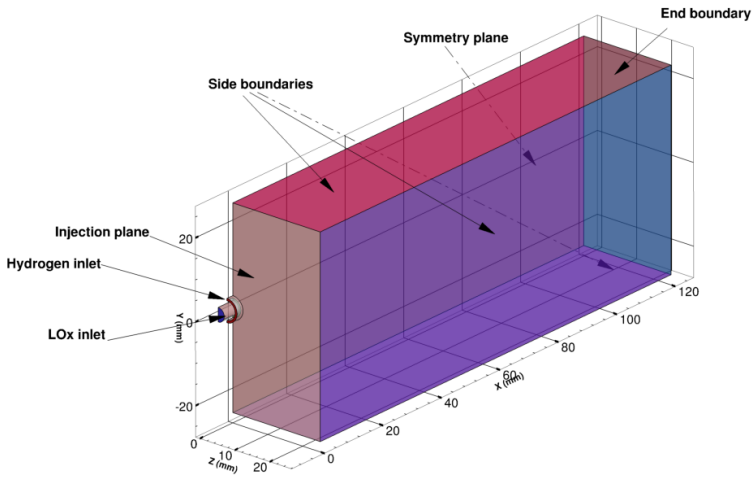

(a) Boundary conditions and 3D half domain

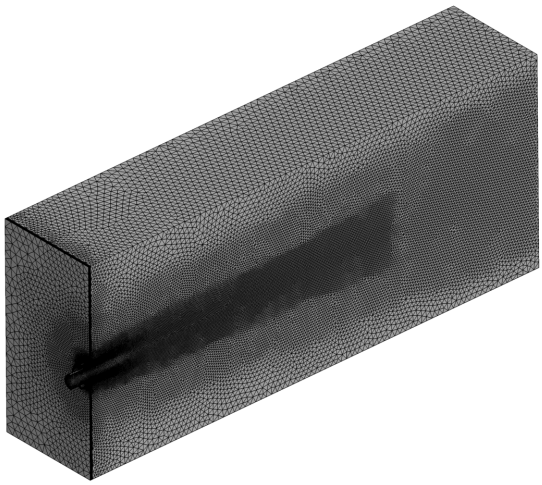

(b) Mesh of the half domain configuration

Figure 10: Half domain configuration

3.2.2 Steady state results

The same kind of analysis of the pressure excitation case is performed. Figure 12 shows a comparison of the three cases for density and OH mass fractions. There is no difference in the length of the LOx core between the two configurations using an unstructured mesh, whereas the hybrid mesh configuration shows a considerably longer one. Table 5 summarises the characteristics.

Table 5: LOx core characteristics

	Half domain	**3D hybrid**	**3D unstructured**
Lenght of the LOx core at $\rho = 100\ kg/m^3$	≈63 mm	≈68 mm	≈6 3mm
Lenght of the LOx core at $\rho = 10\ kg/m^3$	≈65 mm	≈70 mm	≈65 mm
L/D	≈18.5	≈20	≈18.5

For the OH mass fraction distributions, the same considerations between the unstructured and structured meshes already discussed in section 3.1.2 the shear layer can be done. Despite a mesh with less nodes downstream the transition zone, the shear layer presents anyway a good resolution without losses with respect to the fully unstructured case.

DOI: 10.13009/EUCASS2019-559

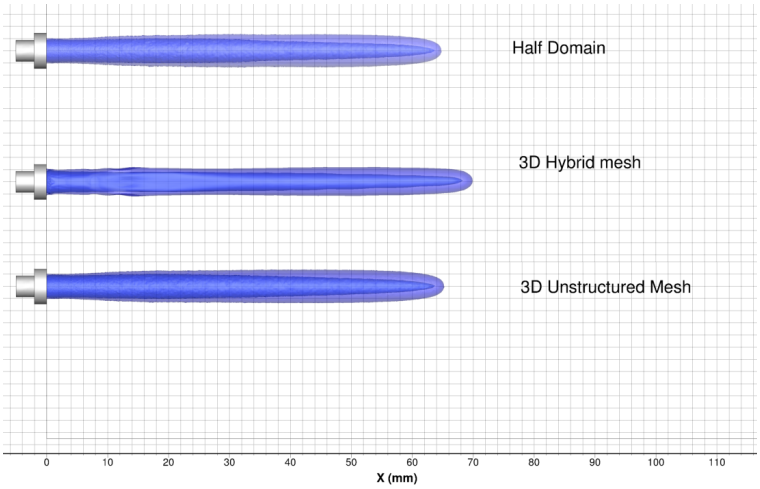

(a) Density isosurfaces at $\rho = 10\ kg/m^3$ and $\rho = 100\ kg/m^3$

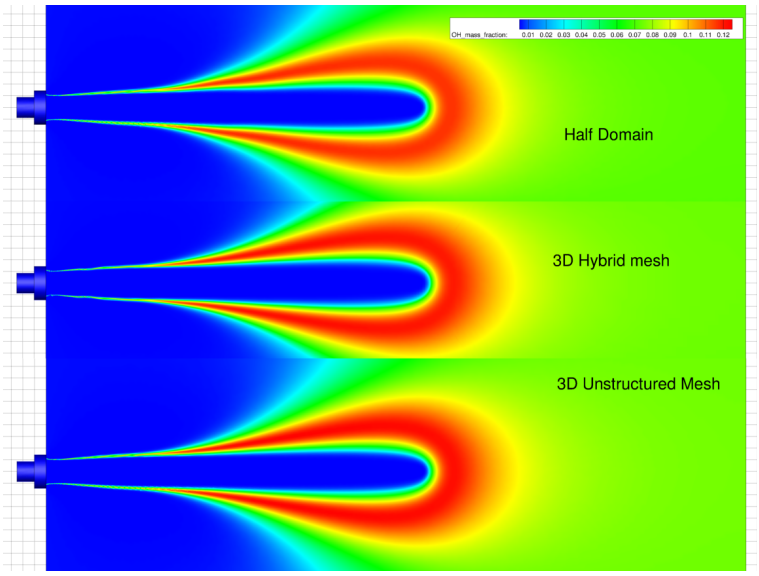

(b) OH mass fraction distribution

Figure 12: Density isosurfaces 12(a) and OH mass fraction distribution 12(b) for the three different configurations.

3.2.3 Excitation results

The transverse velocity excitation produces a shortening and spreading of the LOx core in the spanwise direction, following the trend of the experimental data. The shortening and spreading of the LOx core is displayed in Figure 13. No substantial difference can be noticed, except for the slightly rounder shape of the density distribution. The full domain distribution appears slightly wider and shorter than the half domain one, mantaining the overall characteristics. The main difference is instead in the heat release distribution integrated over the volume, as shown in Figure 14, where the overall evolution and a detail at steady state fluctuations is shown. Table 6 summarizes the main difference in terms of mean value of the heat release and relative difference between the half and full domain configuration. The second line of the table in particular quantifies the difference in the amplitude of the heat release rate fluctuations of the full domain with respect to the half one in terms of relative amplitude with respect to the peaks of the two distributions. This can be again explained by the fact that the axisymmetry boundary condition uses a first order numerical scheme, whereas the field is resolved with a second order one. A first order upwind scheme uses one upstream point for the computations, assuming the face values being identical to the cell values. A second order upwind scheme uses two upstream points and Taylor series are used to evaluated the values at the cell interface from the solution obtained at cell centroid, resulting in higher accuracy.

DOI: 10.13009/EUCASS2019-559

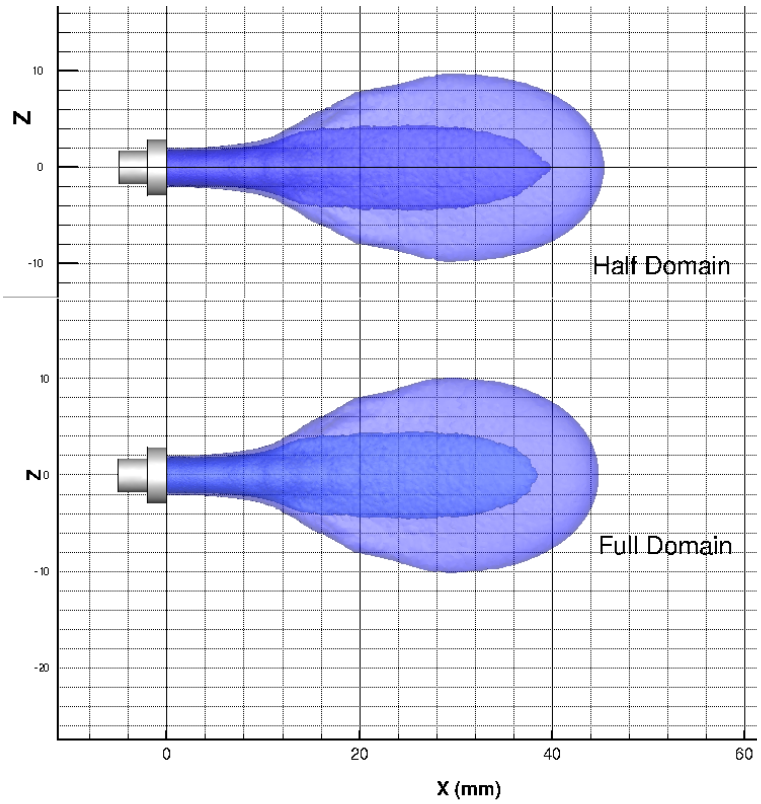

Figure 13: Density isosurfaces at $\rho = 10\ kg/m^3$ and $\rho = 100\ kg/m^3$

Table 6: Heat release fluctuations (%)

	Half domain	**Full domain**
Difference of mean value [a]	+1%	+6.2%
Relative at steady-state fluctuations (peak-to-peak)	reference	+3%

[a]Compared to initial steady state solution

A similar situation as for the pressure velocity excitation is displayed in Figure 14. The heat release both at peak and at steady state regime results to be higher in the full domain, with a higher amplitude fluctuations with respect to the steady state value, with the shape of the fluctuation which is substantially the same. With respect to the half domain, at peak of the steady state fluctuations, an increase of about 2% in the amplitude can be observed. It is to be carefully considered that in this case the only difference is in the geometry of the domain, which has been simply mirrored, as well as the mesh. This difference in the heat release distribution has to be charged on the axyisymmetry boundary condition.

4. Conclusions and outlook

The influence of the numerical setup on the simulation of pressure and transverse velocity excitation of transcritical flames. From the simulation results, an influence of the axisymmetry boundary condition is evident. This boundary condition is a first order one, whereas the solver uses a second order spatial reconstruction. This leads to a discrepancy in the amplitude of the heat release fluctuations, where in the cases where a symmetry axis (pressure excitation) or symmetry plane (transverse velocity excitation) there is an underestimation of the amplitude of the fluctuations. Also the mesh structure has an effect. In the cases where the hybrid mesh is used, the LOx core results to be longer lying in the structured part of the mesh, getting closer to the values given in the experimental data. Starting from this results, next steps will include the investigation of the 1L1T mode excitation for the single injector configuration, which is excited at a frequency of about 5500 Hz in BKH, using an hybrid mesh and trying to calibrate an offset to exploit the symmetry boundary condition, saving computational resources. Then, a full 3D simulation of BKH will be performed

DOI: 10.13009/EUCASS2019-559

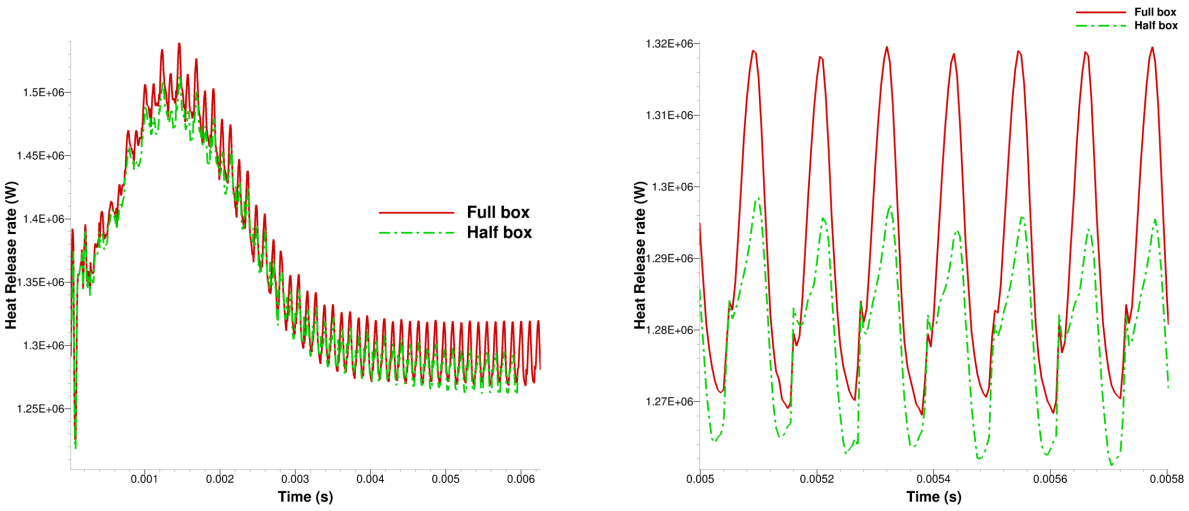

(a) (b)

Figure 14: Comparison of integrated heat release fluctuations in different geometries

for the most relevant load points, trying to avoid the drawbacks of the axisymmetry boundary condition and using a hybrid mesh for the calculations.

5. Acknowledgments

The present work was conducted in the framework of the German Aerospace Center (DLR) project TAUROS (TAU for Rocket Thrust Chamber Simulation) focusing on the qualification and advancement of the DLR flow solver TAU for liquid rocket thrust chamber applications. The financial support of the DLR Space Research Programmatic is highly appreciated. Special thanks go to Tim Horchler and Stefan Fechter, who are always ready to give their support, fixing bugs and improving the functionalities of the TAU Code. This work is also associated with the Franco-German Rocket Engine Stability Initiative (REST).

References

[1] A.Mack and V.Hannemann. Validation of the unstructured dlr tau-code for hypersonic flows. In *Proceedings od the 32nd AIAA Fluid Dynamics Conference and Exhibit*, number AIAA-2002-3111, St.Louis, Missouri, 2013.

[2] A.Urbano, L.Selle, G.Staffelbach, B.Cuenot, T.Schmitt, S.Ducruix, and S.Candel. Exploration of combustion instability triggering using large eddy simulation of a multiple injector liquid rocket engine. *Combustion and Flame*, 2016.

[3] S Beinke, Daniel Banuti, Justin Hardi, M Oschwald, and Bassam Dally. Modeling of a coaxial liquid oxygen/gaseous hydrogen injection element under high-frequency acoustic disturbances. In *Progress in Propulsion Physics*, volume 11, pages 225–246, 02 2019.

[4] Joseph C. Oefelein. Thermophysical characteristics of shear-coaxial lox–h2 flames at supercritical pressure. *Proceedings of the Combustion Institute*, 30:2929–2937, 01 2005.

[5] L. Crocco. Aspects of combustion instability in liquid propellant rocket motors. part 1: Fundamental low frequency instability with monopropellants. *Journal of the American Rocket Society*, Vol .21(6):pp. 163–178, 1951.

[6] D.Banuti. Thermodynamic analysis and numerical modeling of supercritical injection, 2015.

[7] D.Banuti and K.Hannemann. Efficient multiphase rocket propellant injection model with high quality equation of state. In *Proceedings of of the 4th Space Propulsion Conference*, 2014.

[8] D.Banuti, P.C.Ma, J.-P.Hickey, and M.Ihme. Sub- or supercritical? a flamalet analysis for high-pressure rocket propellant injection. In *52nd AIAA/SAE/ASEE Joint Propulsion Conference*, 2016.

DOI: 10.13009/EUCASS2019-559

[9] D.Schwamborn, T.Gerhold, and V.Hannemann. *On the Validation of the DLR-TAU Code*, chapter 72, pages 426–433. New Results in Numerical and Experimental Fluid Mechanics, 1999. Notes on Numerical Fluid Mechanics.

[10] D.T.Banuti, V.Hannemann, K.Hannemann, and B.Weigand. An efficient multi-fluid mixing model for real gas reacting flows in liquid propellant rocket engines. *Combustion and Flame*, (168):98–112, 2016.

[11] Daniel Durox, Thierry Schuller, Nicolas Noiray, and S Candel. Experimental analysis of nonlinear flame transfer functions for different flame geometries. *Proceedings of The Combustion Institute - PROC COMBUST INST*, 32:1391–1398, 12 2009.

[12] Freitag E. *On the Measurement and Modelling of Flame Transfer Functions at Elevated Pressure*. PhD thesis, Technische Universität München, 2009.

[13] Stefan Fechter, Sebastian Karl, Volker Hannemann, and Klaus Hannemann. Simulation of lox/gh2 single coaxial injector at high pressure conditions. In *53rd AIAA/SAE/ASEE Joint Propulsion Conference*, July 2017.

[14] F.Tonti, J.S.Hardi, S.Karl, and M.Oschwald. Unsteady modelling of LOX/GH_2 flame response to longitudinal chamber mode forcing. In *AIAA/SAE/ASME/ASEE Joint Propulsion Conference and Exhibit*, Cincinnati,OH, July 9-12 2018.

[15] R.L Gaffney, J.A.White, S.S.Girinaji, and P.Drummond. Modeling turbulent/chemistry interactions using assumed pdf methods. In *AIAA/SAE/ASME/ASEE Joint Propulsion Conference and Exhibit*, Nashville,TN, July 6-8 1992.

[16] G.Lacaze and J.C.Oefelein. A non-premixed combustion model based on flame structure analysis at supercritical pressures. *Combustion and Flame*, 159:2087–2103, 2012.

[17] Manuel Gonzalez-Flesca, Thomas Schmitt, Sébastien Ducruix, and Sébastien Candel. Large eddy simulations of a transcritical round jet submitted to transverse acoustic modulation. *Physics of Fluids*, 28:055106, 05 2016.

[18] G.Ribert, N.Zong, V.Yang, L.Pons, N.Darabiha, and S.Candel. Counterflow diffusion flames of general fluids: Oxygen/hydrogen mixtures. *Combustion and Flame*, 154(3):319–330, 2008.

[19] Stefan Gröning, Justin Hardi, D Suslov, and M Oschwald. Injector-driven combustion instabilities in a hydrogen/oxygen rocket combustor. *Journal of Propulsion and Power*, 32:1–14, 04 2016.

[20] Layal Hakim, Thomas Schmitt, Sébastien Ducruix, and Sébastien Candel. Dynamics of a transcritical coaxial flame under a high-frequency transverse acoustic forcing: Influence of the modulation frequency on the flame response. *Combustion and Flame*, 162(10):3482 – 3502, 2015.

[21] D.T. Harrje and F.H. Reardon. Liquid propellant rocket combustion instability. *NASA SP-194*, Washingtion D.C., 1972.

[22] Guangbin He, Yanhu Guo, and Andrew T. Hsu. The effect of schmidt number on turbulent scalar mixing in a jet-in-crossflow. *International Journal of Heat and Mass Transfer*, 42(20):3727 – 3738, 1999.

[23] T. Horchler, W. Armbruster, J. Hardi, S. Karl, K. Hannemann, A. Gernoth, and M. De Rosa. Modeling combustion chamber acoustics using the dlr tau code. *Space Propulsion 2018*, 2018.

[24] J.Bellan. Theory,modeling and analysis of turbulent supercritical mixing. *Combustion Science and Technology*, (178):253–281, 2006.

[25] J.C.Oefelein. Mixing and combustion of cryogenic oxygen-hydrogen shear-coaxial jet flames at supercritical pressure. In *Combustion Science and Technology*, number 178, pages 49–100, 2006.

[26] J.S.Hardi, R.Kaess, F.Tonti, P.N.Blanco, S.Soller, M.Oschwald, A.Gernoth, and M.De Rosa. Study of the influence of operating conditions on lox/H_2 thrust chamber acoustic eigenmodes. In *Space Propulsion Conference 2018*, Sevilla, Spain, 13-18 May 2018.

[27] Scott K. Beinke, Justin Hardi, M Oschwald, Daniel Banuti, Sebastian Karl, and Bassam Dally. Experimental and numerical study of oxygen-hydrogen rocket flame response to transverse acoustic excitation. In *Joint Propulsion Conference*, 07 2018.

DOI: 10.13009/EUCASS2019-559

[28] H. J. Krediet, C. H. Beck, W. Krebs, S. Schimek, C. O. Paschereit, and J. B. W. Kok. Identification of the flame describing function of a premixed swirl flame from les. *Combustion Science and Technology*, 184(7-8):888–900, 2012.

[29] E. W. Lemmon, I.H. Bell, M. L. Huber, and M. O. McLinden. NIST Standard Reference Database 23: Reference Fluid Thermodynamic and Transport Properties-REFPROP, Version 10.0, National Institute of Standards and Technology, 2018.

[30] M.Dumbser, U.Iben, and C.D.Munz. Efficient implementation of high order unstructured weno schemes for cavitating flows. *Computer&Fluids*, (86):141–168, 2013.

[31] M.Oschwald, J.J.Smith, R.Branam, J.Hussong, A.Schik, B.Cheroudi, and D.Talley. Injection of fluids into supercitical environments. *Combustion Science and Technology*, (178):49–100, 2006.

[32] C.-C. Rossow. Extension of a compressible code toward the incomproessible limit. *AIAA Journal*, (41):2379–2386, 2003.

[33] Ideen Sadrehaghighi. Mesh generation in cfd, 05 2019.

[34] S.Beinke, F.Tonti, S.Karl, J.Hardi, M.Oschwald, and B.Dally. Modelling flame response of a co-axial LOx/GH_2 injection element to high frequency acoustic forcing. *7th European Conference for Aeronautics and Aerospace Sciences (EUCASS)*, 2017.

[35] S.K.Beinke. *Analysis of Flame Response to Acoustic Forcing In a Rocket Combustor*. PhD thesis, School of Mechanical Engineering, The university of Adelaide, South Australia 5005, Australia, April 2017.

[36] P. Spalart and S. Allmaras. *A one-equation turbulence model for aerodynamic flows*.

[37] T.Gerhold, O.Friedrich, J.Evans, and M.Galle. Calculation of complex three-dimensional configurations employing the dlr-tau-code. *AIAA Paper*, pages 97–0167, 1997.

[38] Hasret Turkeri, Stephen B. Pope, and Metin Muradoglu. A les/pdf simulator on block-structured meshes. *Combustion Theory and Modelling*, 23(1):1–41, 2019.

[39] Annafederica Urbano, Quentin Douasbin, Laurent Selle, Gabriel Staffelbach, Bénédicte Cuenot, Thomas Schmitt, Sébastien Ducruix, and Sébastien Candel. Study of flame response to transverse acoustic modes from the les of a 42- injector rocket engine. *Proceedings of the Combustion Institute*, 36(2):2633–2639, 2017.

[40] V. Yang and W. Anderson. Liquid rocket engine combustion instability. *Progress in Astronautics and Aeronautics*, Vol. 169, AIAA, Washington D.C, 1995.